We are IntechOpen, the world's leading publisher of Open Access books Built by scientists, for scientists

6,900
Open access books available

186,000
International authors and editors

200M
Downloads

Our authors are among the

154
Countries delivered to

TOP 1%
most cited scientists

12.2%
Contributors from top 500 universities

CLARIVATE ANALYTICS
BOOK CITATION INDEX
INDEXED

WEB OF SCIENCE™

Selection of our books indexed in the Book Citation Index
in Web of Science™ Core Collection (BKCI)

Interested in publishing with us?
Contact book.department@intechopen.com

Numbers displayed above are based on latest data collected.
For more information visit www.intechopen.com

OCT with a Visible Broadband Light Source Applied to High-Resolution Nondestructive Inspection for Semiconductor Optical Devices

Nobuhiko Ozaki, Kazumasa Ishida, Tsuyoshi Nishi, Hirotaka Ohsato, Eiichiro Watanabe, Naoki Ikeda and Yoshimasa Sugimoto

Abstract

Optical coherence tomography with a visible broadband light source (vis-OCT) was developed for high-resolution and nondestructive measurements of semiconductor optical devices. Although a near-infrared (NIR) light source should be used for medical OCT to obtain deep penetration of biological samples, a visible broadband light source is available as a low-coherence light source for industrial products. Vis-OCT provides higher axial resolution than NIR-OCT, because the axial resolution of an OCT image is proportional to the square of the center wavelength of the light source. We developed vis-OCT with an axial resolution of less than 1 μm in air and obtained cross-sectional profiles and images of ridge-type waveguides having heights and widths of several μm. Additionally, we performed cross-sectional measurements and imaging of a stacked semiconductor thin layer. The measured values were similar to those measured by scanning electron microscopy, and the effectiveness of vis-OCT for nondestructive inspection of semiconductor optical devices was demonstrated.

Keywords: vis-OCT, nondestructive inspection, optical device fabrication, semiconductor optical device, high-resolution imaging
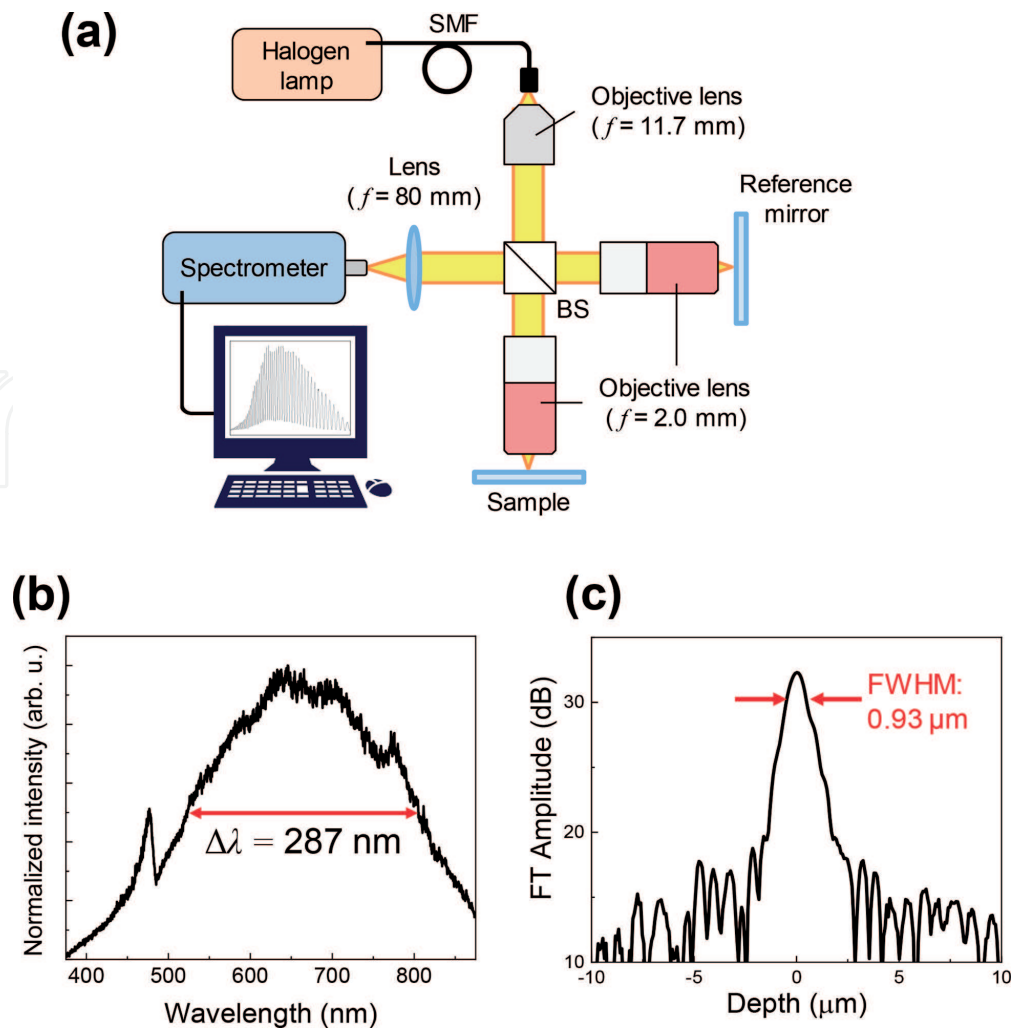
1. Introduction

Nondestructive inspection technologies have become mandatory for fabrication and evaluation of various industrial products [1]. In particular, as products are miniaturized into μm and nm scales, high-resolution measurement methods are necessary. For semiconductor optical devices, photonic integrated circuits (PICs) [2] have been developed from the recent progress of fabrication techniques. For the PICs, highly dense optical devices are connected using optical waveguides [e.g., ridge-type optical waveguides (RWGs)] having several to sub-μm scales to

propagate light [3, 4]. Thus, the structural accuracy of the fabricated waveguides becomes significant for reducing their propagation loss and increasing PIC efficiency and reliability. The waveguides are typically carved on semiconductor materials using fine-processing technologies such as photolithography and dry etching [5]. To optimize the process conditions, it is necessary to measure the thickness of a photoresist coating on semiconductor wafers: several to sub-µm. Furthermore, the fabricated waveguides should be inspected as designed. To measure the photoresist thickness or fabricated waveguides, scanning electron microscopy (SEM) or step profiler has been frequently used [6]. However, these measurement methods are destructive or require contact with the sample. Development of a nondestructive and non-contact measurement method with a high spatial resolution is thus required.

Optical techniques enable nondestructive, contactless characterization of thin films. For instance, ellipsometry [7] is commonly used to measure thicknesses of thin films. However, it has a relatively large spot size (>40 µm) and is not suitable for a lateral local measurement of wafers. On the other hand, an optical cross-sectional imaging technique, called optical coherence tomography (OCT) [8], has been developed. OCT is commonly used in medical fields (e.g., ophthalmology). It is based on low-coherence interferometry, and the reflectivity profile of a sample along an optical axis can be obtained using a focused probe. By scanning the probe in the lateral directions, two-dimensional (2D) and three-dimensional (3D) profile imaging can be achieved. The axial resolution of an OCT image is governed by the central wavelength (λ_0) and bandwidth ($\Delta\lambda$) of the low-coherence light source. The axial resolution can be expressed as $0.44\lambda_0^2/\Delta\lambda$ when a broadband light source has a Gaussian spectral shape [9]. For conventional medical OCT, λ_0 should be in the near-infrared (NIR) range to allow deep penetration of biological samples [10, 11]. However, when industrial products are observed by OCT, a visible broadband light can be used as an OCT light source, and the axial and lateral resolutions of an OCT image can be further improved beyond that of the NIR-OCT images, owing to the shorter λ_0. For instance, when the λ_0 is 650 nm and $\Delta\lambda$ is beyond 200 nm, the axial resolution can be expected to be less than 1 µm. This value is comparable to the dimension of optical semiconductor devices included in PICs. Furthermore, the visible-range optical components, such as light source and detector, are widely used and are relatively cost-effective, and there are many options. Therefore, we developed vis-OCT as a nondestructive high-resolution inspection tool [12, 13]. In this chapter, the vis-OCT system and its inspections of optical components, semiconductor-based optical waveguides, polymer-based integrated patterns, and semiconductor thin film are introduced.

2. Spectral-domain OCT with a visible broadband light source

A spectral-domain (SD)-OCT [14], having a visible broadband light, was constructed as shown in **Figure 1(a)**. SD-OCT, categorized as a Fourier-domain OCT [15], enables a distribution of spatial reflectivities along the optical axis through an inverse Fourier-transformed (IFT) spectrum of interference among reflections from the sample and a reference mirror. We utilized a halogen lamp unit (ANDO AQ4305) coupled with a single-mode fiber of ~4.0 µm core diameter as the visible broadband light source. The integrated output power from the SMF in the visible spectral range was approximately 220 nW. The introduced light was collimated using an objective lens (*f* = 11.7 mm) and split by a beam splitter (BS) into sample and reference arms. Each split light was focused on the sample and the reference

Figure 1.
(a) Schematic of the Vis-OCT setup. (b) Spectrum of the light source in the Vis-OCT. (c) PSF obtained from the IFT interference spectrum between the reflections from the reference and sample mirrors. (Reprinted with permission from Ref. [13]. Copyright 2018, The Japan Society of Applied Physics).

mirror by a high numerical aperture (0.50) objective lens with a plan apochromatic aberration correction from visible to near-infrared wavelength region (Mitutoyo M Plan Apo NIR 100×) (f = 2.0 mm). By using this objective lens, the spot size of each focused beam could be reduced, estimated to be approximately 0.68 μm in diameter without degradation of the axial resolution caused by aberrations. The reflections from the sample and the reference mirror were recombined at the BS, and the interfered signal was focused by an achromatic lens (f = 80 mm) into the spectrometer. The interference spectrum was detected by the spectrometer (Ocean Optics USB4000) with a Si-based charge-coupled device detector (3648 pixels) with an exposure time of approximately 100 ms. By calculating the IFT interference spectrum, a depth profile of the sample along the optical axis was obtained [16]. A 2D OCT image was then produced by scanning the probe light in steps of 0.2 μm in the lateral direction.

    Figure 1(b) shows a spectrum of the light source reflecting from the reference mirror detected with the spectrometer. The center wavelength was approximately 662 nm, and the full width at half maximum (FWHM) was approximately 287 nm. The axial resolution of the SD-OCT system can be estimated from the point spread function (PSF) of the light source obtained from the IFT interference spectrum between the reflections from the reference mirror and an identical mirror set on the sample stage. The PSF of the light source is presented in **Figure 1(c)**, and the FWHM of the PSF, which corresponds to the axial resolution, was approximately 0.93 μm.

3. Surface-structure observations and measurements of RWGs and periodic patterns with Vis-OCT
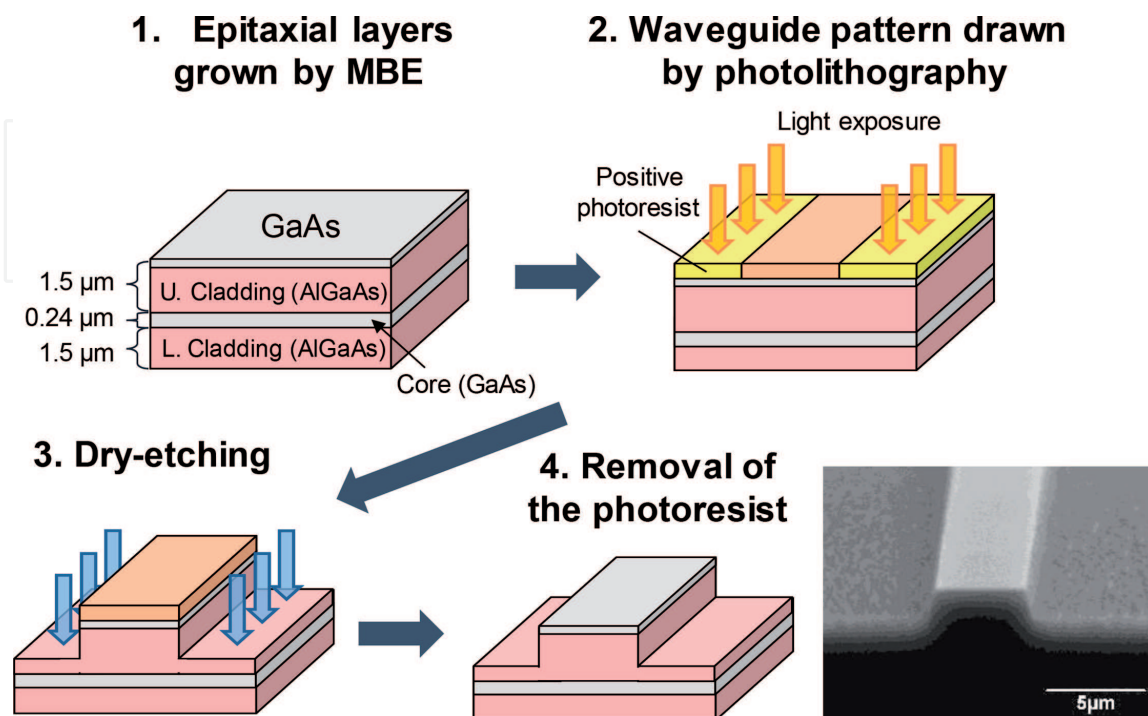
We first measured optical waveguides and periodic patterns as typical optical device components to evaluate the axial and lateral resolutions of developed vis-OCT. In this section, the performance of the vis-OCT for surface-structure measurement and observation is described.

3.1 Sample preparations

For the test samples of surface-structure observations, we prepared semiconductor-based straight RWGs. The RWG was formed on typical optical confinement layers, which consisted of a core layer of GaAs and upper- and lower-cladding layers of AlGaAs [17]. After the epitaxial growth of the semiconductor layers on a GaAs substrate via molecular beam epitaxy (MBE), RWGs were separately fabricated on the wafer with 1.5-μm nominal height and various nominal widths (3–100 μm) using conventional photolithography and dry etching processes (**Figure 2**).

We prepared periodic patterned structures fabricated on a soft mold made of polydimethylsiloxane (PDMS) with several to sub-μm scale for nano-imprint lithography (NIL) [18], as shown in **Figure 3**. Three laterally periodic patterns, line and space (L/S), hexagonal lattice pillars, and hexagonal lattice holes, were formed on the soft mold with nominal 4-μm pitch and 0.5-μm height (or depth). These are typically designed for optical micro- and nano-waveguides, photonic crystal structures, or micro-channels for lab-on-a-chip, etc. We investigated the capability of the vis-OCT with these high-dense patterns for lateral and axial high-resolution measurements.

The light probe was introduced from the above sample surface and scanned in-plane direction across the RWG or periodic patterns to obtain the depth profile and profile images.
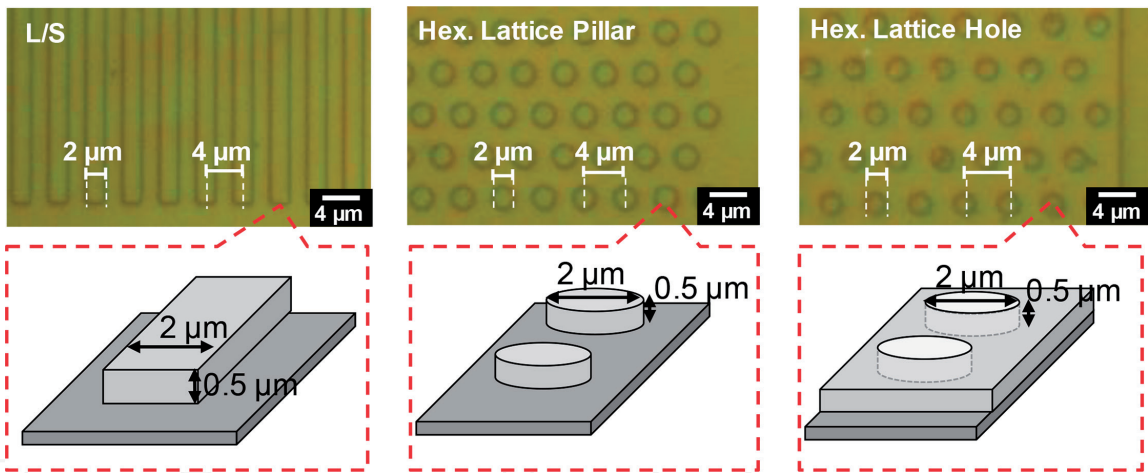

Figure 2.
Schematic of semiconductor RWG fabrication processes and a typical SEM image of the fabricated RWG with a nominal width of 3 μm. (Reprinted with permission from Ref. [13]. Copyright 2018, The Japan Society of Applied Physics).
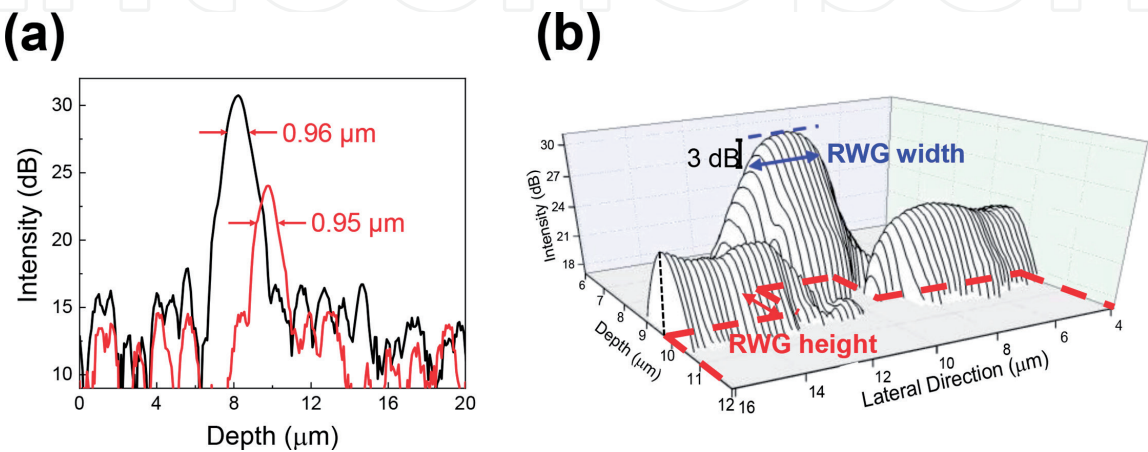
3.2 Height and width measurements of isolated RWGs

Figure 4(a) shows depth profile curves obtained with a probe fixed on the RWG (black line) and the substrate aside the RWG (red line) [13]. Each profile indicates a peak with a line width of approximately 0.95–0.96 μm, which can be caused by the reflection from the surfaces of the RWG and the substrate, and the line width almost corresponds to that of the PSF of the light source, as shown in **Figure 1(c)**. The peak intensity at the surface of the substrate was smaller (approximately −5 dB) than that at the surface of the RWG. This might have resulted from a reduction in the back reflection caused by light scattering at the dry-etched rough surface. The peak positions at the surfaces were shifted, suggesting that the RWG height can be estimated from the peak-shift value. From this case, the RWG height was estimated at ~1.52 μm. We then obtained the depth profile curves by scanning with the light probe at intervals of 0.2 μm in the lateral direction across the RWG with 3-μm width and summarized the profile curves in **Figure 4(b)**.

As seen in **Figure 4(b)**, the reflection peaks at the surfaces of the substrate and the RWG can be clearly distinguished. At the boundary between the RWG and the substrate, the incident light probe spanned both surfaces, and the signal intensities were overlapped in a short range of the lateral direction. Thus, we defined the boundary position where the peak intensity dropped 3 dB from the peak intensity of the RWG surface. Based on the depth profile curves, signal intensity was scaled

Figure 3.
Optical microscopic and schematics of soft molds for NIL with various lateral patterns.
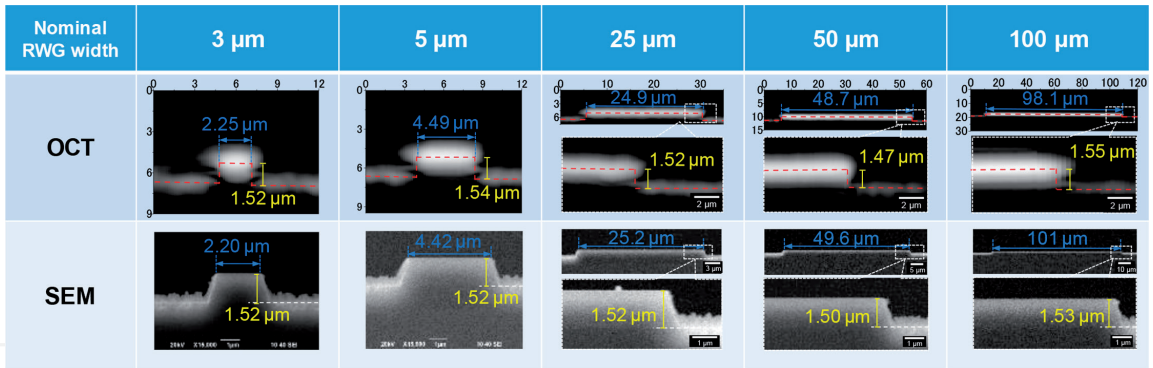

Figure 4.
(a) Depth profile curves obtained from the surface of the RWG with 3-μm width (black line) and the substrate (red line). (b) Summarized profile curves. (Reprinted with permission from Ref. [13]. Copyright 2018, The Japan Society of Applied Physics).

on an 8-bit grayscale, where white denotes maximum and black denotes minimum, and a cross-sectional OCT image was constructed. **Figure 5** summarizes the OCT images obtained from RWGs with various widths and cross-sectional SEM images of the RWGs obtained from a cleaved edge. The surface line of the substrate and the RWG indicated by a red dashed line in each OCT image was determined at the reflection peak position. The RWG height and width measured by vis-OCT correspond well with the values measured via SEM observation. **Figure 6(a), (b)** shows the comparison of the measured heights and widths of various RWGs between vis-OCT and SEM.
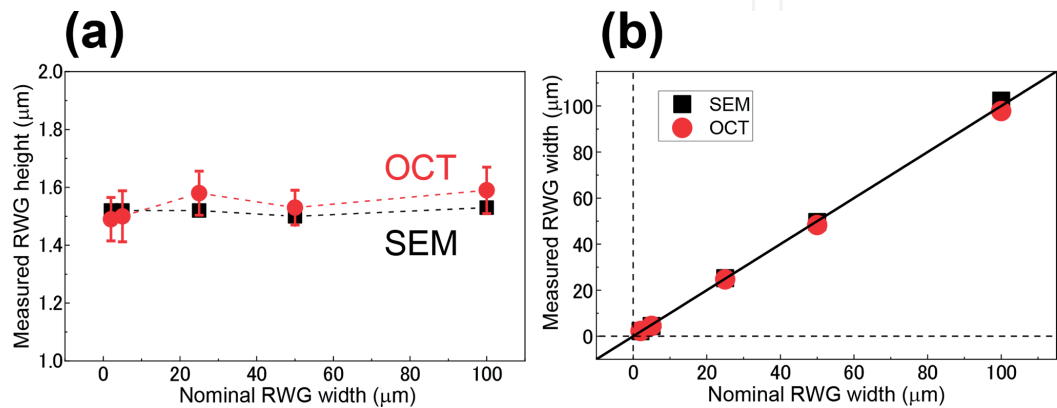
3.3 Soft mold for NIL

We then observed soft molds with periodically integrated patterns, such as line and space, hexagonal lattice of pillars, and holes. **Figure 7** shows optical microscopic (plan-view) and vis-OCT (cross-sectional) images of the molds. The OCT images clearly show the profile image of the periodic patterns, indicating the height and pitch of the patterns. Despite the slight variation of dimensions, the measured height and depth of approximately 0.5 μm and the pitch of approximately 4 μm were reasonable values.

These results demonstrated the effectiveness of the vis-OCT for measurements and imaging of integrated structures with several to sub-μm scale. Furthermore, the mold is made of polymer (PDMS) and difficult to be observed by SEM because of charging. Vis-OCT can avoid the problem and realize nondestructive and high-resolution inspection even for the polymer-based material.
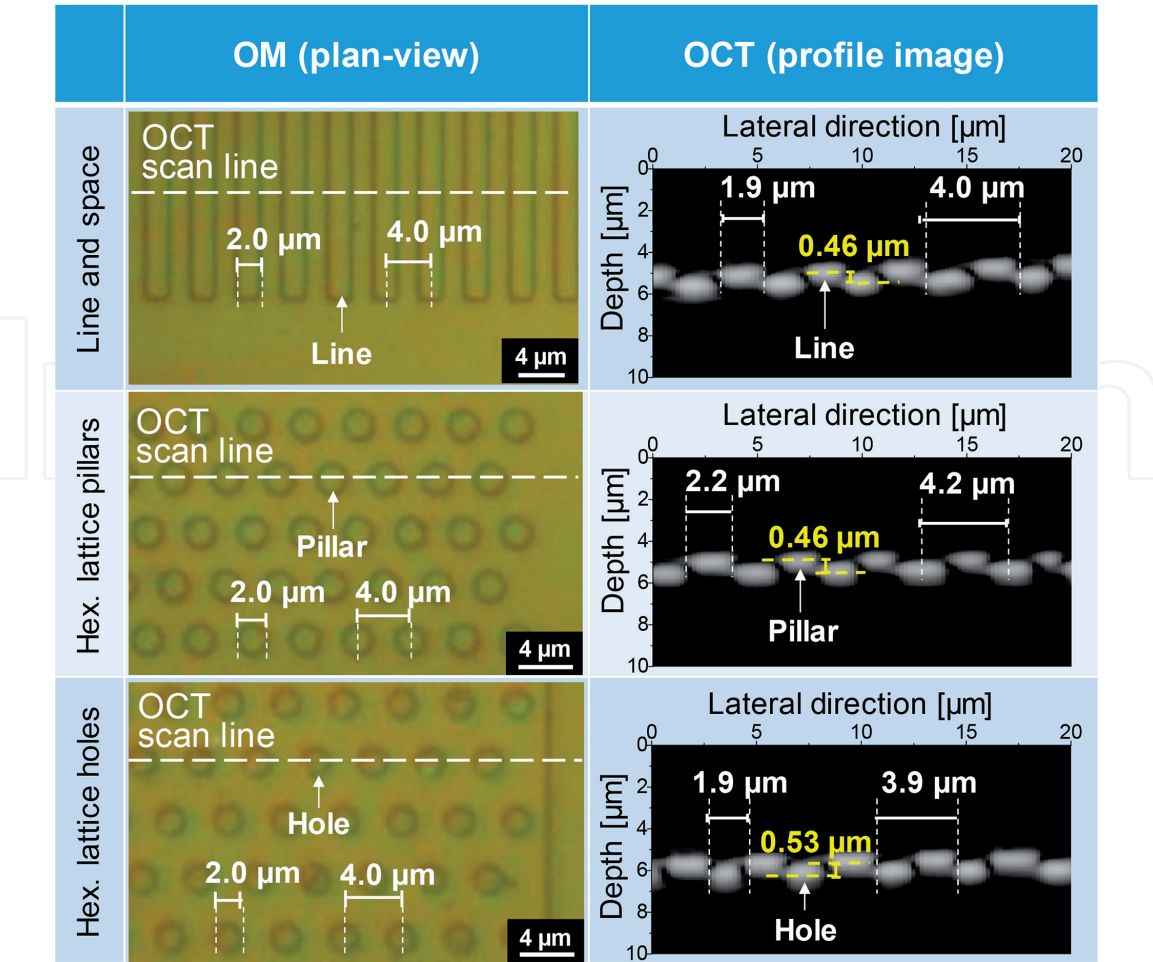

Figure 5.
Comparison of profile images using Vis-OCT and SEM for RWGs with various widths.

Figure 6.
Summarized measured values of (a) height and (b) width of RWGs with various nominal widths using Vis-OCT and SEM. (Reprinted with permission from Ref. [13]. Copyright 2018, The Japan Society of Applied Physics).

Figure 7.
NIL soft-mold profile images obtained via Vis-OCT and plan-view images with an optical microscope.

4. Profile imaging of semitransparent thin films

As shown in the previous section, the availability of the vis-OCT was demonstrated for nondestructive inspection for surface structures with high axial resolution (less than 1 μm) and lateral resolution (less than 2 μm). We then attempted to obtain a profile imaging of stacked layers underneath the sample surface. Generally, thin semiconductor layers are stacked in optical devices, and an inspection method for the layer embedded in a device, such as the thickness or interface flatness of the layers, is beneficial. Although a layer of transparency for visible light can be easily imaged with vis-OCT, a nontransparent or partial transparent layer, which is an optical absorbent layer for a whole or partial of the visible light, should be difficult to be measured. In this section, our proposed method to determine the physical thickness of such a layer using the vis-OCT is introduced.

4.1 Sample of stacked thin layers

An epitaxial AlGaAs thin layer was grown on a GaAs wafer by MBE as a test sample. As shown in **Figure 8**, a nominal 0.5-μm-thick $Al_{0.35}Ga_{0.65}As$ layer was prepared and was coated with an approximately 2-μm-thick layer of photoresist (AZ 5214E, Microchemicals GmbH). The cross-sectional SEM image was obtained from a cleaved sample edge. A photoresist layer is typically spin-coated before patterns are drawn with a photolithography process. The measurement of thickness of the photoresist layer is important for optimizing the condition of pattern drawing. The refractive index of the photoresist layer (n_{pr}) was approximately 1.62 for
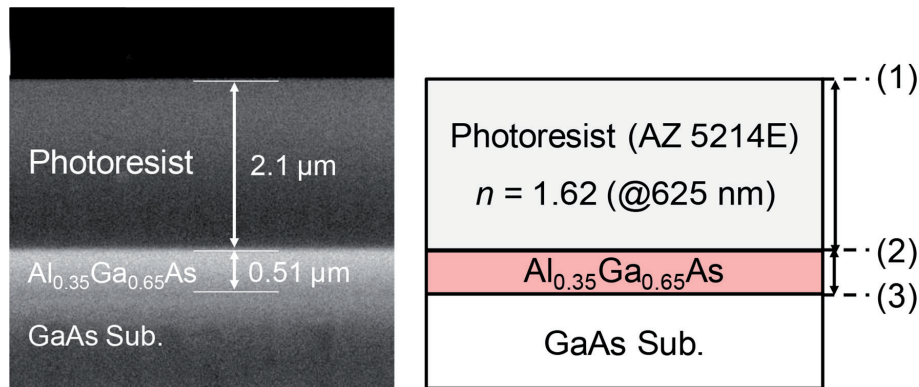
625-nm light, and there is not a large dispersion of n_{pr} for visible light (1.61–1.66 for λ = 830–400 nm) [19], as shown in the lower part of **Figure 9(a)**. The physical thickness of the photoresist film, therefore, can be estimated from the optical thickness divided by n_{pr}.
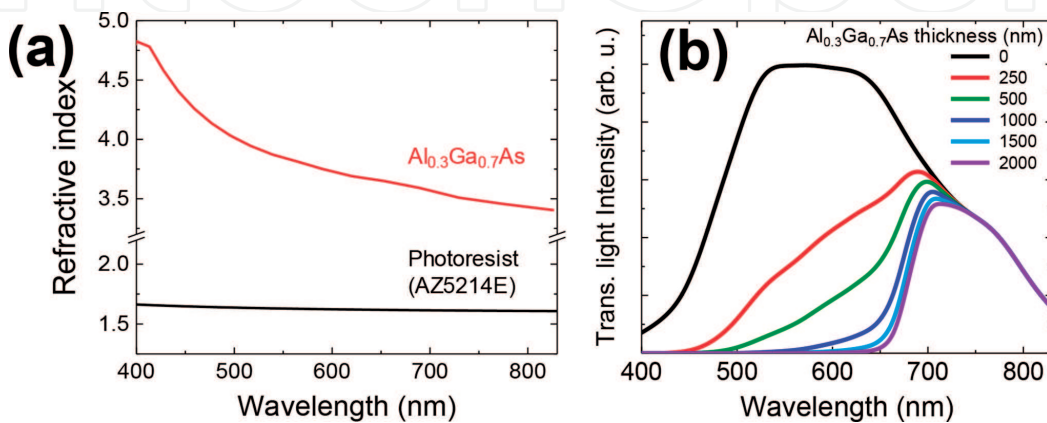
Measuring the AlGaAs layer thickness is also important, because the etched AlGaAs layer thickness should be monitored when the RWG is fabricated, as shown in **Figure 2**. However, the refractive index of AlGaAs (n_{AlGaAs}) has a large dispersion, unlike the photoresist layer. The refractive index of the $Al_{0.3}Ga_{0.7}As$ layer varies in the range of 3.5–4.8 as a function of the wavelength of visible broadband light, as shown in the upper part of **Figure 9(a)**. Moreover, the $Al_{0.3}Ga_{0.7}As$ layer exhibits optical absorbance, depending on the wavelength, because of the bandgap energy. **Figure 9(b)** presents simulated spectra of the visible broadband light source transmitted through an $Al_{0.3}Ga_{0.7}As$ layer with various thicknesses in the range of 250–2000 nm. This indicates variations of the transmitted spectral shape of the visible broadband light with the thickness of the $Al_{0.3}Ga_{0.7}As$ layer resulting in the variation of n_{AlGaAs} with the spectral changes.

4.2 Numerical simulations

As described in the previous section, the semiconductor layer has a dispersion relation of its refractive index, and the transmitted spectrum is varied with the thickness of the layer. Thus, it should be difficult to determine the physical thickness of the

Figure 8.
Cross-sectional SEM image and profiles of a fabricated sample. (Reprinted with permission from Ref. [12]. Copyright 2016, The Japan Society of Applied Physics).
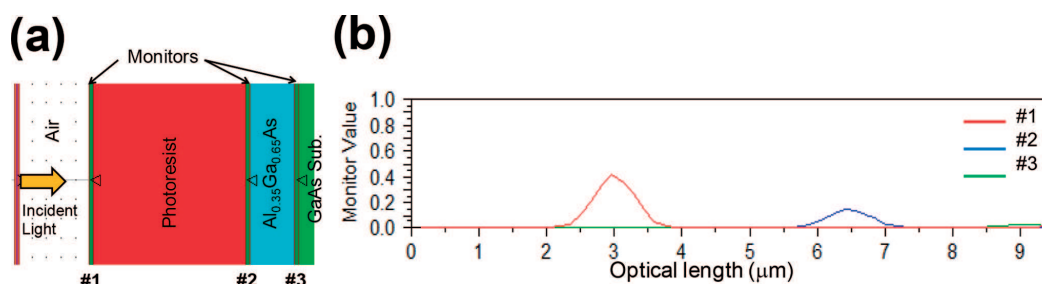

Figure 9.
(a) Dispersion refractive indices of $Al_{0.3}Ga_{0.7}As$ and photoresist. (b) Simulated transmitted spectra through $Al_{0.3}Ga_{0.7}As$ films with various thicknesses. (Reprinted with permission from Ref. [12]. Copyright 2016, The Japan Society of Applied Physics).

AlGaAs layer from a value of optical thickness obtained with vis-OCT. To determine the physical thickness of thin semiconductor layers, we propose the utilization of numerical simulations based on the finite-difference time-domain (FDTD) method [20, 21]. This simulation provides the propagation of an optical wave of visible broadband light in the sample. The FDTD method is a time-domain simulation for modeling electrodynamics and is useful for predictions of light propagation in a wide frequency range in an arbitrary material. The variations in intensity and shape of a spectrum as broadband light travels in the material can be numerically reproduced based on successive calculations of Maxwell's equations in time and space. This enables the estimation of a precise optical length of a broadband light beam traveling in a material having wavelength dispersion of optical absorbance and refractive index.
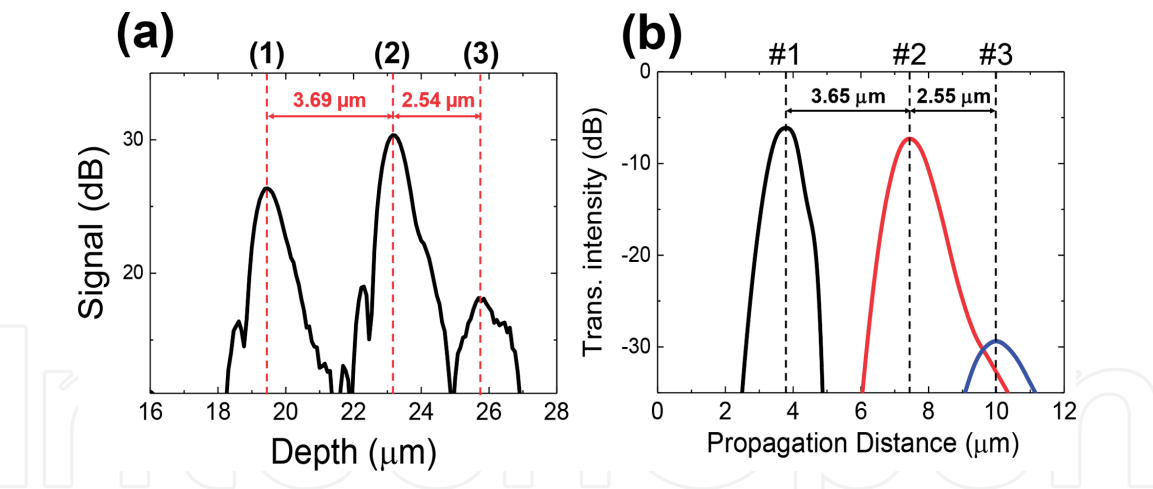
We executed the FDTD simulation on a 2D model using commercial software (Rsoft Design Group, FullWAVE). As shown in **Figure 10(a)**, a 2D model of stacked layers was prepared, and a pulse light was introduced from the left side of the model. **Figure 10(b)** shows plots of intensity of the incident pulse recorded as a function of time (converted to optical length) at each layer boundary (#1–3). The appearance of peaks in the plot indicates that the light propagated, and the distance between two peaks indicates a traveling length of light corresponding to an optical thickness of the layer. We calculated the optical thickness for simulation models with different physical thicknesses of the AlGaAs layer set around 500 nm. The calculated optical thickness was then compared with the optical thickness experimentally obtained via vis-OCT. The physical thickness was determined as a corresponding thickness set in the simulation model.

4.3 Profile measurements and imaging with the Vis-OCT

Figure 11(a) shows the depth profile of the sample obtained with the vis-OCT. Three clear peaks appear in the profile, which can be attributed to reflections at the boundaries of each layer: (1) the surface of the photoresist, (2) the interface between the photoresist and AlGaAs layer, and (3) the interface between the AlGaAs layer and the GaAs substrate. The distance between peaks (1) and (2) of the sample is 3.69 μm, which is nearly the same as the product (3.4 μm) of the photoresist thickness (2.1 μm) and its approximate n_{pr} of 1.62. Considering that the OCT depth profiles indicate the optical path lengths, peaks (1) and (2) can be interpreted as reflections at the surface and at the interface of the photoresist layer. However, the distance between peaks (2) and (3) cannot be analyzed in the same manner, because the refractive index of AlGaAs is not predictable, as described in the previous section. We thus compared the experimental value with the FDTD simulations for models having various values of physical thickness of the AlGaAs layer. The simulation result, which provided the most comparable optical length, is shown in **Figure 11(b)**. The physical thickness of the AlGaAs layer was set at 512 nm in

Figure 10.
(a) 2D model for the FDTD simulation. (b) Example of the recorded incident light intensity at layer boundaries #1–3. (Reprinted with permission from Ref. [12]. Copyright 2016, The Japan Society of Applied Physics).
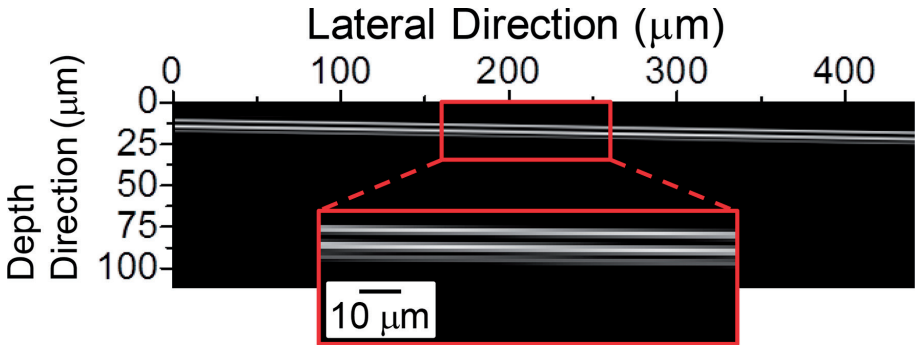
Figure 11.
(a) Depth profile of the sample obtained via Vis-OCT. (b) FDTD simulation result obtained from the most comparable optical length to the experimentally measured profile. (Reprinted with permission from Ref. [12]. Copyright 2016, The Japan Society of Applied Physics).

the simulation model, and the propagation distance (optical length) between layer boundaries #2 and #3 was 2.55 μm. The physical thickness of 512 nm in the model is close to the value measured by the cross-sectional SEM (0.51 μm), as shown in **Figure 8**, demonstrating the effectiveness of the proposed method.

The above results show that vis-OCT, combined with the FDTD simulation, is useful for the profile measurement of not only a transparent film but also the optically absorbent epitaxial semiconductor layer. Although the sample cleaved for the SEM observation was the same wafer used in the vis-OCT measurements, the site for vis-OCT measurement was not at exactly the same position. Thus, the thickness of the grown layer might have been slightly different. Additionally, the visible broadband light spectrum used in the FDTD simulation had an ideal Gaussian shape (symmetric at the central wavelength), which is different from the actual spectrum of the light source used in vis-OCT. This difference in spectral shape should have affected the simulation result, and further optimization of the FDTD simulation parameter could have increased the accuracy.

Furthermore, we obtained a 2D profile image of the sample by collecting profiles in a lateral direction, as shown in **Figure 12**. This image clearly shows the cross-sectional structure of the sample, which could be utilized for inspecting the homogeneity of the film thickness and lateral structures after the etching process. In particular, the clear visualization of the boundary between the AlGaAs and GaAs layers should be useful when a ridge-type waveguide is fabricated on the wafer, because precise measurements of the height of the waveguide and the distance between the bottom

Figure 12.
Profile image of the sample with the Vis-OCT. (Reprinted with permission from Ref. [12]. Copyright 2016, The Japan Society of Applied Physics).

of the waveguide and the GaAs active layer are important requirements for attaining high transmission efficiency in the waveguide. These results demonstrate the effectiveness of vis-OCT for high-resolution, nondestructive profile measurement and imaging in the fabrication of semiconductor optical devices.

5. Conclusions

We demonstrated a nondestructive and non-contact inspection for semiconductor optical devices using vis-OCT with high axial and lateral resolutions of less than 1 µm. Profiles of RWGs and patterned soft molds were obtained, and measurements of the heights and widths of the structures were performed. Furthermore, the physical thickness measurements of an opaque epitaxially grown AlGaAs layer were demonstrated by combining the vis-OCT with FDTD-based numerical simulation. These results offer a novel application of OCT for nonmedical fields.

Acknowledgements

Conflict of interest

The authors declare no conflict of interest.

Author details

Nobuhiko Ozaki[1*], Kazumasa Ishida[1], Tsuyoshi Nishi[1], Hirotaka Ohsato[2], Eiichiro Watanabe[2], Naoki Ikeda[2] and Yoshimasa Sugimoto[2]

1 Wakayama University, Wakayama, Japan

2 National Institute for Materials Science, Tsukuba, Ibaraki, Japan

*Address all correspondence to: ozaki@wakayama-u.ac.jp

IntechOpen

References

[1] Dwivedi SK, Vishwakarma M, Soni A. Advances and researches on non destructive testing: A review. Materials Today: Proceedings. 2018;**5**:3690-3698. DOI: 10.1016/j.matpr.2017.11.620

[2] Coldren LA, Corzine SW, Mashanovitch ML. Diode Lasers and Photonic Integrated Circuits. 2nd ed. Hoboken, NJ: Wiley; 2012

[3] Rickman A. The commercialization of silicon photonics. Nature Photonics. 2014;**8**:579-582. DOI: 10.1038/nphoton.2014.175

[4] Pogossian SP, Vescan L, Vonsovici A. The single-mode condition for semiconductor rib waveguides with large cross section. Journal of Lightwave Technology. 1998;**16**:1851-1853. DOI: 10.1109/50.721072

[5] Xiao H. Introduction to Semiconductor Manufacturing Technology. 2nd ed. Bellingham, WA: SPIE Press; 2012

[6] Stout KJ, Blunt L. Three-Dimensional Surface Topography. 2nd ed. London: Penton Press; 2000

[7] Tompkins HG, Irene EA. Handbook of Ellipsometry. Norwich, NY: William Andrew publishing; 2005

[8] Huang D, Swanson EA, Lin CP, Schuman JS, Stinson WG, Chang W, et al. Optical coherence tomography. Science. 1991;**254**:1178-1181. DOI: 10.1126/science.1957169

[9] Brezinski ME. Optical Coherence Tomography: Principles and Applications. New York: Academic Press; 2006

[10] Patterson MS, Wilson BC, Wyman DR. The propagation of optical radiation in tissue. II: Optical properties of tissues and resulting fluence distributions. Lasers in Medical Science. 1991;**6**:379-390. DOI: 10.1007/BF02042460

[11] Salomatina E, Yaroslavsky AN. Evaluation of the in vivo and ex vivo optical properties in a mouse ear model. Physics in Medicine and Biology. 2008;**53**:2797-2807. DOI: 10.1088/0031-9155/53/11/003

[12] Nishi T, Ozaki N, Oikawa Y, Miyaji K, Ohsato H, Watanabe E, et al. High-resolution and nondestructive profile measurement by spectral-domain optical coherence tomography with a visible broadband light source for optical-device fabrication. Japanese Journal of Applied Physics. 2016;**55**:08RE05. DOI: 10.7567/JJAP.55.08RE05

[13] Ishida K, Ozaki N, Ohsato H, Watanabe E, Ikeda N, Sugimoto Y. Non-destructive and non-contact measurement of semiconductor optical waveguide using optical coherence tomography with a visible broadband light source. Japanese Journal of Applied Physics. 2018;**57**:08PE03. DOI: 10.7567/JJAP.57.08PE03

[14] De Boer JF. Spectral/Fourier domain optical coherence tomography. In: Drexler W, Fujimoto JG, editors. Optical Coherence Tomography: Technology and Applications. New York: Springer; 2008. pp. 147-175

[15] Fercher AF, Hitzenberger CK, Kamp G, El-Zaiat SY. Measurement of intraocular distances by backscattering spectral interferometry. Optics Communication. 1995;**117**:43-48. DOI: 10.1016/0030-4018(95)00119-S

[16] Shibata H, Ozaki N, Yasuda T, Ohkouchi S, Ikeda N, Ohsato H, et al. Imaging of spectral-domain optical coherence tomography using a superluminescent diode based on InAs

quantum dots emitting broadband spectrum with Gaussian-like shape. Japanese Journal of Applied Physics. 2015;**54**:04DG07. DOI: 10.7567/ JJAP.54.04DG07

[17] Yasuda T, Ozaki N, Shibata H, Ohkouchi S, Ikeda N, Ohsato H, et al. Electrically driven near-infrared light source with Gaussian-like broadband spectral shape by using multiple self-assembled InAs quantum dots with controlled emission wavelengths. IEICE Transactions on Electronics. 2016;**E99-C**:381-384. DOI: 10.1587/transele. E99.C.381

[18] Chou SY, Krauss PR, Renstrom PJ. Imprint lithography with 25-nanometer resolution. Science. 1996;**272**:85-87. DOI: 10.1126/science.272.5258.85

[19] MicroChemicals photoresists product spec. Available from: http:// www.microchemicals.com/technical_ information/photoresists_optical_ parameters.pdf

[20] Yee K. Numerical solution of initial boundary value problems involving Maxwell's equations in isotropic media. IEEE Transactions on Antennas and Propagation. 1966;**14**:302-307. DOI: 10.1109/TAP.1966.1138693

[21] Taflove A. Application of the finite-difference time-domain method to sinusoidal steady-state electromagnetic-penetration problems. IEEE Transactions on Electromagnetic Compatibility. 1980;**22**:191-202. DOI: 10.1109/TEMC.1980.303879